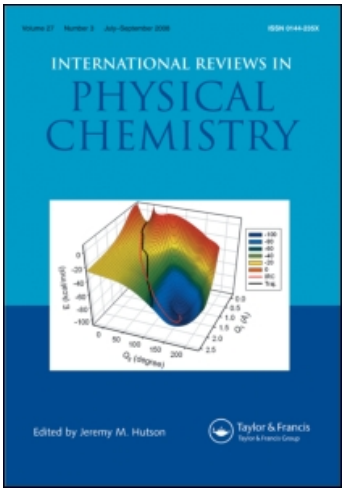

International Reviews in Physical Chemistry
Publication details, including instructions for authors and subscription information:
http://www.informaworld.com/smpp/title~content=t713724383

Vibrational energy in molecules probed with high time and space resolution

Yoonsoo Pang[a]; John C. Deàk[b]; Wentao Huang[c]; Alexei Lagutchev[a]; Andrei Pakoulev[d]; James E. Patterson[e]; Timothy D. Sechler[f]; Zhaohui Wang[a]; Dana D. Dlott[a]
[a] School of Chemical Sciences, University of Illinois at Urbana Champaign, Urbana, IL 61801 [b] Department of Chemistry, University of Scranton, Scranton, PA 18510 [c] Cooperative Instititue for Research in Environmental Sciences, University of Colorado, Boulder, CO 80309 [d] Department of Chemistry, University of Wisconsin, Madison, WI 53706 [e] Institute for Shock Physics, Washington State University, Pullman, WA 99164 [f] Department of Chemistry, University of Pennsylvania, Philadelphia, PA 19104

To cite this Article Pang, Yoonsoo , Deàk, John C. , Huang, Wentao , Lagutchev, Alexei , Pakoulev, Andrei , Patterson, James E. , Sechler, Timothy D. , Wang, Zhaohui and Dlott, Dana D.(2007) 'Vibrational energy in molecules probed with high time and space resolution', International Reviews in Physical Chemistry, 26: 1, 223 — 248
To link to this Article: DOI: 10.1080/01442350601084091
URL: http://dx.doi.org/10.1080/01442350601084091

International Reviews in Physical Chemistry,
Vol. 26, No. 1, January–March 2007, 223–248

Taylor & Francis
Taylor & Francis Group

Vibrational energy in molecules probed with high time and space resolution

YOONSOO PANG†, JOHN C. DEÀK‡, WENTAO HUANG§, ALEXEI LAGUTCHEV†, ANDREI PAKOULEV¶, JAMES E. PATTERSON‖, TIMOTHY D. SECHLER⊥, ZHAOHUI WANG† and DANA D. DLOTT*†

†School of Chemical Sciences, University of Illinois at Urbana Champaign, Urbana, IL 61801
‡Department of Chemistry, University of Scranton, Scranton, PA 18510
§Cooperative Instititue for Research in Environmental Sciences, University of Colorado, Boulder, CO 80309
¶Department of Chemistry, University of Wisconsin, Madison, WI 53706
‖Institute for Shock Physics, Washington State University, Pullman, WA 99164
⊥Department of Chemistry, University of Pennsylvania, Philadelphia, PA 19104

(*Received 21 September 2006; in final form 14 October 2006*)

This article reviews experimental measurements of vibrational energy in condensed-phase molecules that simultaneously provide time resolution of picoseconds and spatial resolution of ångströms. In these measurements, ultrashort light pulses are used to input vibrational energy and probe dynamical processes. High spatial resolution is obtained using vibrational reporter groups in known locations on the molecules. Three examples are discussed in detail: (1) vibrational energy flow across molecules in a liquid from an OH– group to a CH_3– group; (2) vibrational energy flow across a molecular surfactant monolayer that separates an aqueous and a non-polar phase in a suspension of reverse micelles; and (3) vibrational energy input by laser-driven shock waves to a self-assembled monolayer of long-chain alkane molecules. These experiments provide new insights into the movement of mechanical energy over short length and time scales where ordinary concepts of heat conduction no longer apply, where the concepts of quantum mechanical energy transfer reign supreme.

Contents

*Corresponding author. Email: dlott@scs.uiuc.edu

International Reviews in Physical Chemistry
ISSN 0144–235X print/ISSN 1366–591X online
http://www.tandf.co.uk/journals
DOI: 10.1080/01442350601084091

1. Introduction

Heat transport is a significant factor in virtually every condensed-phase mechanical and chemical process. In a bit of oversimplification, in macroscopic objects heat is transported by acoustic phonons whose energies are less than kT, where k is Boltzmann's constant [1, 2]. These phonons frequently scatter off defects, resulting in diffusive heat transport over distances greater than the mean-free path. At the nanoscale and below, conventional concepts of heat transfer may no longer apply [3]. One must instead invoke the concepts of quantum-mechanical vibrational energy transfer (VET). Individual molecules have specific, quantized vibrational energy levels, and the energies of most of these levels are much greater than kT, so VET processes are inherently quantum mechanical. The rules that govern VET in condensed-phase molecules and in molecular materials are at present not very well understood. Vibrational excitations have short lives (typically decaying on the ps time scale), and these lifetimes are controlled by anharmonic interactions with other vibrations [4–7]. The motion of vibrations through physical space may involve a mixture of coherent (wavelike) and incoherent (diffusive) transport. VET is a fundamental process in molecular science for which there is a clear lack of knowledge [8]. The lack of knowledge stems from the difficulty of experimental measurements and theoretical calculations [9]. Vibrational excitations in condensed phases are difficult to produce and difficult to probe [9], while molecular simulations confront the daunting problem [10] of a quantum mechanical system immersed in a many-particle bath.

One of the most significant developments in the study of vibrational energy came shortly after the development of the picosecond laser. At the University of Munich in the 1970 s, W. Kaiser and A. Laubereau developed numerous methods for pumping and probing vibrational excitations in liquids [6]. In their initial experiments, the only wavelengths available were the Nd:glass fundamental and harmonic (1.064 μm and 0.532 μm). Vibrations were excited by stimulated Raman scattering and probed by either coherent or incoherent Raman scattering [6]. Incoherent probe measurements are much more difficult, but in contrast to coherent probes which measure vibrational dephasing, incoherent probes provide direct access to the excited-state populations of the pumped or 'parent' state and subsequently excited 'daughter' states. Another important development was the generation of ultrashort tunable infrared (IR) pulses [11]. IR pulses are much more efficient for pumping vibrational transitions because a typical Raman cross-section is $10^{-31}\,m^2\,Sr^{-1}$, whereas a typical IR cross-section is $10^{-22}\,m^2$. Experiments where ultrashort IR pulses are used to pump and probe

molecular vibrations have led to a revolution in experimental studies of VET in condensed phases [8, 12]. The combination of IR pumping and incoherent Raman probing, first demonstrated by Spanner *et al*. [13] and now used extensively in the Dlott laboratory, is technically much more difficult, but its ability to simultaneously probe the instantaneous populations of both parent and daughter vibrations confers unique advantages as will be seen below.

One of the most significant developments in the study of interfacial vibrations occurred in 1987, when groups at Bell Laboratories and at Berkeley introduced the technique of vibrational sum-frequency generation (SFG) spectroscopy. The use of SFG for vibrational spectroscopy of interfacial layers is by now well-known and has been the subject of many reviews (e.g. [14–20]). Since SFG is a three-photon process that vanishes in centrosymmetric media (in the dipole approximation), at the interface of two such media the signal arises from interfacial species alone. About a decade later, broadband multiplex SFG techniques were introduced [21, 22]. In broadband multiplex SFG, a broadband femtosecond pulse in the vibrational IR is combined with a narrowband picosecond visible pulse to generate a coherent sum-frequency signal, which evidences enhanced (or depleted) intensities at interfacial vibrational resonances. With broadband SFG, complete SFG spectra with time resolutions of about 1 ps can be obtained with individual laser shots, which makes it possible to study ultrafast processes at surfaces and interfaces, a unique combination of high temporal and spatial resolution of vibrational energy [23].

In this review, we present examples of recent work from the Dlott lab employing either the IR-Raman technique or broadband SFG, where vibrational energy has been studied with high time and space resolution. Time resolution follows in a natural way from the ultrashort durations of the pump and probe pulses. Space resolution of ångströms requires more explanation, since the diffraction limit precludes such resolution with visible or IR wavelengths. In our research, spatial resolution follows from a foreknowledge of the molecular or material structure, coupled with the use of vibrational reporters that are mainly localized on a single atomic group [24, 25]. The examples to be described here are illustrated in figure 1. In figure 1(a), vibrational

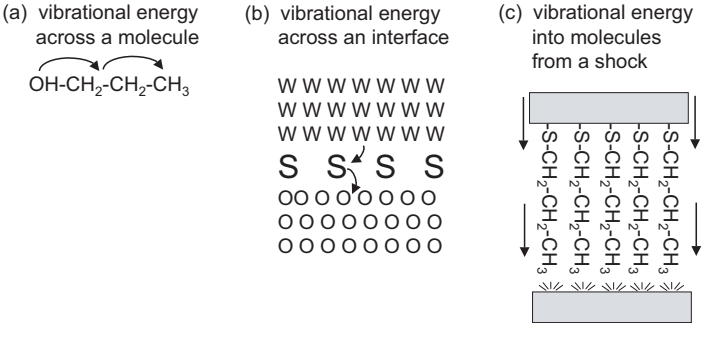

Figure 1. Vibrational energy with high time and space resolution: examples to be discussed. (a) Vibrational energy moving across a molecule in a liquid. (b) Vibrational energy moving across a surfactant interface; w = water, S = surfactant, O = organic solvent. (c) Vibrational energy input to long-chain alkane self-assembled monolayers (SAM) via shock compression.

energy flows across a molecule in a liquid. An IR pulse was used to excite a stretching excitation of the hydroxyl (OH–) group and a Raman probe was used to monitor stretching excitations of the methyl (CH_3–) group on the opposite end of the molecule [25]. In figure 1(b), vibrational energy flows across an interfacial surfactant monolayer (S) separating an aqueous (w) and an organic (o) phase [24]. An IR pulse excited stretching transitions of water confined near the interface and a Raman probe monitored vibrational excitations of the surfactant monolayer and the organic liquid. In figure 1(c), vibrational excitations were pumped into a monolayer of a long-chain alkanethiol molecules (self-assembled monolayer, SAM) using a femtosecond laser-driven shock wave. An SFG probe monitored the orientation of the terminal methyl group of the chains, which indicated whether the chains undergo bending, or mechanical failure caused by the generation of *gauche* defects [26].

2. Three-dimensional IR-Raman spectroscopy

A tunable IR pulse is used to pump a selected vibration and a time-delayed visible probe pulse is used to generate the Raman spectrum. When light at frequency ω_L is inelastically scattered from matter, the Raman spectrum can be broken down into a Stokes and anti-Stokes branch having intensities,

$$\boldsymbol{I}_{ST}(\omega) \propto [n(\omega,T)+1]\sigma_R(\omega)(\omega_L-\omega)^4 \tag{1a}$$

and,

$$\boldsymbol{I}_{AS}(\omega) \propto n(\omega,T)\sigma_R(\omega)(\omega_L-\omega)^4, \tag{1b}$$

where $n(\omega,T)$ is the 'occupation number' given by the Planck distribution function, $n(\omega,T)=[1-\exp(-\hbar\omega/kT)]^{-1}$, and $\sigma_R(\omega)$ is the Raman cross-section [6]. Equation 1(b) shows that the intensity of each anti-Stokes transition is proportional to the occupation number $n(\omega,T)$, and equations 1(a) and 1(b) together show that by combining simultaneous Stokes and anti-Stokes measurements, the cross-section $\sigma_R(\omega)$ can be eliminated to yield the absolute occupation number $n(\omega,T)$. When a pump pulse at frequency ω_{IR} creates a non-equilibrium population, the occupation numbers become time dependent, and anti-Stokes probing with a short-duration pulse combined with a multichannel spectrograph provides the time-dependent occupation numbers $n(\omega,t)$ of all Raman-active vibrations simultaneously. The most important feature of the IR-Raman method is its unique ability to follow the flow of vibrational excitations from the parent vibration to daughter vibrations on the same molecule and on nearby molecules. Subsequent to IR pumping, the irradiated region of material thermalizes (typically in <1 ns) yielding an equilibrium temperature jump ΔT, so as $t\to\infty$, $n(\omega,t)\to n(\omega,T+\Delta T)$. On a much longer time scale during the (1 ms) interval between laser shots, the laser-heated region is either refreshed or it returns to ambient temperature by thermal conduction.

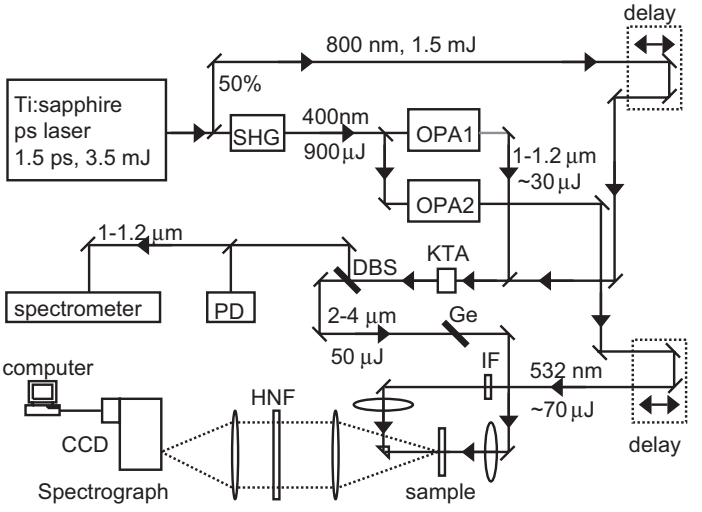

Figure 2. Block diagram of the laser system used for 3D IR-Raman spectroscopy. Key: SHG = second-harmonic generator; OPA = optical parametric amplifier; KTA = potassium titanyl arsenate mixer crystal for mid-IR generation; DBS = dichroic beamsplitter; PD = photodiode; Ge = germanium Brewster window; IF = 25 cm^{-1} FWHM interference filter at 532 nm; HNF = holographic notch filter, CCD = charge-coupled device optical detector. OPA1 is tuned from 1.0 μm to 1.176 μm to produce IR in the 2500–4000 cm^{-1} range, and OPA2 is fixed at 532 nm. Reproduced from ref. [30].

In our laboratory, we have greatly advanced the IR-Raman method using powerful high repetition rate lasers [27–31] based on chirped-pulse amplified Ti:sapphire, computer-controlled optical parametric amplifiers (OPA), and a fast (f/1.4) spectrograph with a multichannel CCD detection system. A block diagram of the IR-Raman experiment [30] is shown in figure 2. The system was designed to provide the frequency resolution needed to probe individual vibrational transitions of molecular liquids and molecular materials where the vibrational linewidths are rarely $< 15\,cm^{-1}$ [27]. The pulse duration corresponding to this resolution is about 1 ps. With this apparatus it becomes possible to obtain three-dimensional spectra [29, 32]. The three dimensions are pump frequency, the frequency (i.e. the Raman shift) of the probed vibration and the delay time. It is thus possible to watch the complete response of molecules and materials to different kinds of vibrational excitations.

An example of such a molecular response is shown in figure 3, where the sample is liquid methanol (CH_3–OH) at ambient temperature [29], and ω_{IR} is tuned either to the CH-stretch transition ν_{CH} or the OH stretch transition ν_{OH}. The molecular response is quite different in these two cases. With ν_{CH} pumping, the parent excitation decays in distinct stages. First ν_{CH} relaxation populates mainly the δ_{CH} bending vibrations. Subsequent decay of δ_{CH} populates mainly the ν_{CO} stretching vibration, whose decay populates lower-energy torsions and collective vibrations of the liquid. These lower energy states were not observed directly, but their dynamics were inferred on the basis of the molecular thermometer measurements discussed below. With ν_{OH} pumping, relaxation of the parent vibration is clearly distinct from the ν_{CH} case. The decay of ν_{OH} excites all intramolecular vibrations simultaneously to different extents, with the predominant product being the δ_{OH} bending vibration [29, 33].

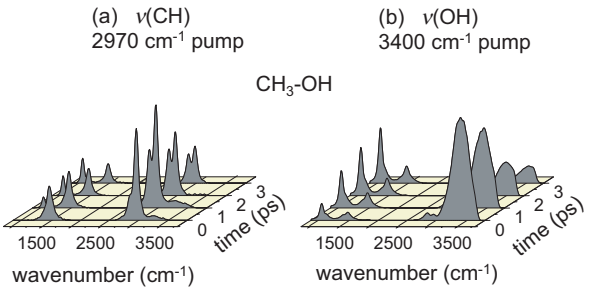

Figure 3. [Colour online] IR-Raman data on liquid methanol at ambient temperature with either CH stretch or OH stretch excitation. A coherent artifact at the (indicated) pump wavenumber has been subtracted away. Reproduced from ref. [29].

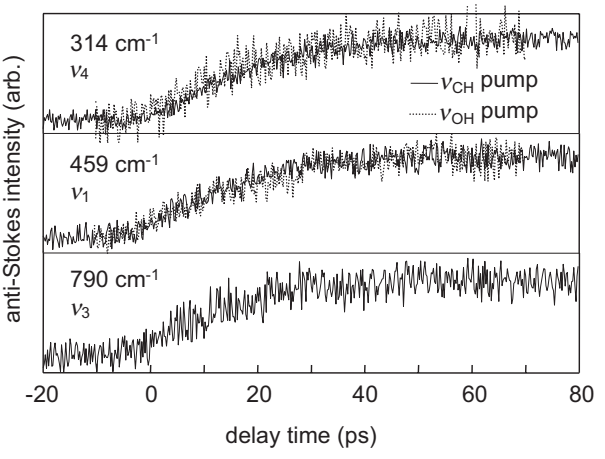

Figure 4. Rise of vibrational excitation from three CCl_4 transitions in methanol:CCl_4 solution (75% methanol, 25% CCl_4). Solid curves are for ν(CH) pumping, dotted curves for ν(OH) pumping. Reproduced from ref. [29].

Within about 20 ps the methanol molecules become thermalized with $\Delta T \approx 20\,\mathrm{K}$. The value of ΔT is determined by the IR laser pulse energy E_p [28],

$$\Delta T = \frac{2E_p\alpha}{\pi r_0^2 \rho C_\mathrm{V}}, \tag{2}$$

where ΔT denotes the temperature rise at the centre of the (approximately) Gaussian laser beam with $(1/e^2)$ beam diameter r_0, α is the absorption coefficient, and ρ and C_V are the density and constant-volume heat capacity. The progress from specific ν_CH or ν_OH excitations toward a thermalized state has been observed by spiking the methanol with CCl_4. The CCl_4 is a molecular thermometer [34]; as the methanol loses energy, the rising temperature of the CCl_4 can be monitored with anti-Stokes scattering. The lower frequency modes of CCl_4 quickly uptake energy from the cooling methanol molecules [34]. As shown in figure 4 [29], the lower frequency vibrations of CCl_4 heat up

simultaneously on the 20 ps time scale, due to efficient redistribution of the vibrational energy among the CCl_4 vibrations [34]. The thermalization process duration is about the same with either ν_{CH} or ν_{OH} pumping.

3. Watching vibrational energy move across a molecule

Figure 3(b) shows that in methanol, the simplest alcohol, most of the energy in ν_{OH} is transferred to lower energy bending and stretching vibrations. Nonetheless a small portion of the vibrational energy in ν_{OH} is transferred to ν_{CH}. This observation foreshadows the opportunity to watch vibrational energy move from a vibrational donor to an acceptor in units of one carbon–carbon bond length (~1.5 Å).

Although VET from a donor to an acceptor on another part of a molecule is reminiscent of electronic energy transfer between dye molecules, for instance dye donor and acceptor pairs anchored to a protein molecule, it is fundamentally quite different. Electronic energy transfer typically involves through-space interactions, such as a dipole–dipole interaction in the case of Förster transfer [35]. Through-space VET is not expected to be significant between OH and CH stretching transitions located a few ångströms apart, because typical vibrational transition dipole moments do not yield energy transfer rates that are competitive with the picosecond time scale vibrational lifetimes.

A diagram of the relevant levels [36, 37] for the examples of ethanol CH_3CH_2OH and 1-propanol $CH_3(CH_2)_2OH$ is shown in figure 5. Because of the energy mismatch for excitation transfer from ν_{OH} to ν_{CH} (~300 cm^{-1}), the $\nu_{OH} \rightarrow \nu_{CH}$ process requires a

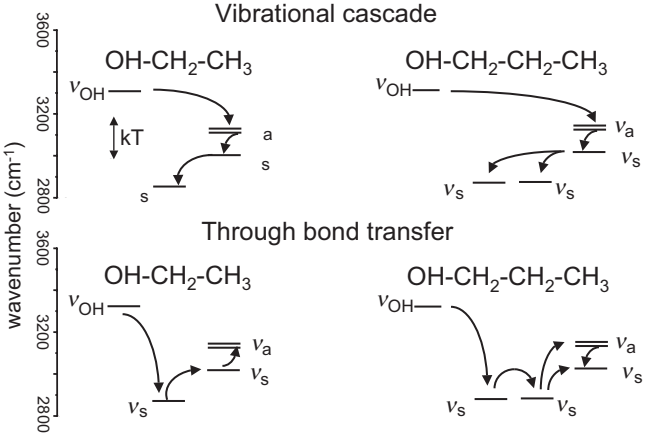

Figure 5. Energy level diagrams for vibrational energy transfer (VET) from OH to CH stretching vibrations of ethanol (left) and 1-propanol (right). Not shown are the lower energy bend and stretch vibrations that are the dominant energy relaxation pathways for excited OH and CH stretching excitations. (Top) If vibrational energy moved downward through the energy levels (vibrational cascade), methyl CH_3 stretching vibrations would be populated before methylene CH_2 vibrations. (Bottom) If through-bond VET were dominant, vibrational energy would move through the intervening methylene vibrations before reaching the methyl group. Reproduced from ref. [25].

solvent bath [5, 38] to uptake or provide the needed energy. In an ambient temperature liquid, steps up or down in energy of a few hundred cm^{-1} are possible [5], because the average thermal energy of the bath $kT = 200\,cm^{-1}$. Energy flow down hydrocarbon chains *isolated* from a thermal bath is possible, but only if ν_{CH} is excited in a higher overtone region where the density of states [39] is much greater than in the fundamental region [40].

Broadly speaking there are two paradigms for excitation energy transfer from ν_{OH} to ν_{CH} of a terminal CH_3 [25]. In a *vibrational cascade* [39], vibrational excitation percolates down the energy levels. If the vibrational cascade were dominant, figure 5 shows that ν_{OH} decay would first excite the higher energy 'a' states $\nu_a(CH_3)$ and $\nu_a(CH_2)$ and then the lower energy 's' states $\nu_s(CH_2)$ and $\nu_s(CH_3)$. ($\nu_a(CH_2)$ is not shown explicitly in figure 1 because this transition is not seen in the Raman or IR spectra of these alcohols.) In physical space this would correspond to a first step of jumping from OH to CH_3 across the intervening methylene groups. In *through-bond transfer*, vibrational excitation would run from OH across the intervening atomic groups, first to CH_2 and then to CH_3. Figure 5 [25] shows that in energy space the through-bond process involves a first step *down in energy* from ν_{OH} to $\nu_s(CH_2)$, followed by steps *up in energy* to $\nu_s(CH_3)$ and $\nu_a(CH_3)$.

The Stokes Raman spectrum of ethanol [25] is shown in figure 6(a). This figure indicates the different stretching transitions and shows that σ_R is about 20 times greater for ν_{CH} than for ν_{OH}. Anti-Stokes transient spectra [25] shown in figure 6(b) were obtained after ν_{OH} excitation at $3300\,cm^{-1}$. In the first one picosecond, the predominant product of ν_{OH} decay in the ν_{CH} region is the CH_2 stretch $\nu_s(CH_2)$. Subsequently the stretching energy in CH_2 moves uphill from $\nu(CH_2)$ to $\nu(CH_3)$. The data in figure 6(b) clearly distinguish between the two possibilities illustrated in figure 5. Energy transfer from ν_{OH} to $\nu(CH_3)$ in ethanol moves from OH first to CH_2 and then to CH_3. We have also been able to show that the OH and CH_3 groups must be *on the same molecule*, as opposed to intermolecular transfer between OH and CH_3

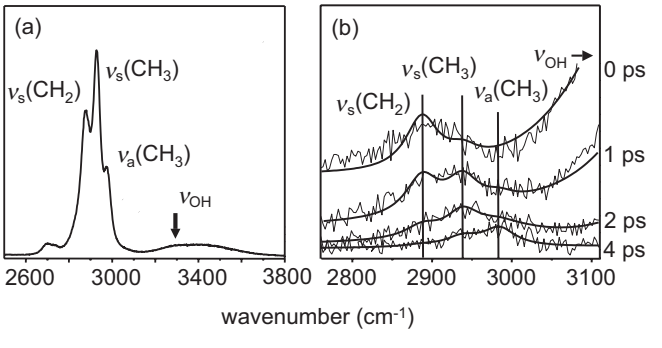

Figure 6. (a) Stokes Raman spectrum of ethanol (liquid, 295 K) showing the OH, CH_3 and CH_2 stretching vibrations. The arrow indicates the wavenumber of the mid-IR pump pulses used to excite OH stretching. (b) Anti-Stokes transient spectra. The computer-generated smooth curves use parameters taken from the Stokes Raman spectrum with variable amplitude factors. The OH excitations pumped by the laser are to the right of the displayed spectra. No more than 1–2% of the OH stretch excitations are transferred to CH stretch excitations. Vibrational excitation is observed to flow from OH first to CH_2, subsequently moving uphill in energy to CH_3, as indicated in the through-bond transfer scheme in figure 5. Reproduced from ref. [25].

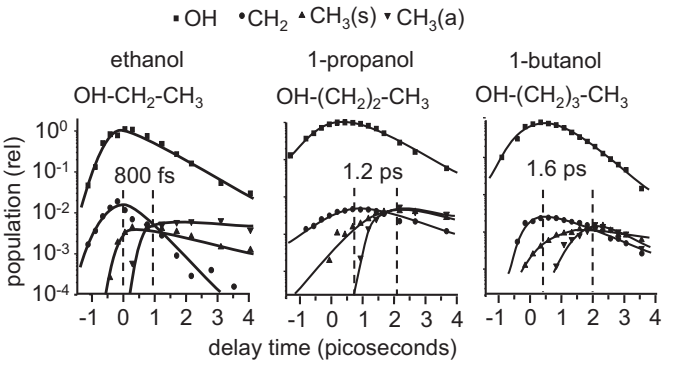

Figure 7. Time-dependent populations after OH stretching excitation of OH and CH stretching vibrations of ethanol (a), 1-propanol (b) and 1-butanol. The vertical line pair in each panel marks the peak of the OH stretch and the 90% point of the CH_3 (a state) populations. The time constant for $OH \rightarrow CH_3$ (a state) transfer increases by about 0.4 ps for each additional intervening CH_2 group. Reproduced from ref. [25].

during a collision between adjacent molecules [25]. This was done by studying *t*-butyl alcohol, OH–C–$(CH_3)_3$. We observed no energy transfer from OH to CH_3 in this liquid. In *t*-butyl alcohol there are no high-frequency CH-stretch modes on the central carbon atom to conduct the higher-frequency components of the vibrational energy. With the intramolecular pathway blocked in this manner, OH-to-CH_3 transfer ceases, ruling out the possibility of intermolecular pathways. Thus the energy transfer process occurs predominantly *via the through-bond mechanism* from OH to CH_2 to CH_3, as opposed to a vibrational cascade down the energy levels from OH to CH_3 to CH_2.

The distance dependence of energy transfer is illustrated [25] in figure 7, where the number of methylene groups was varied from one to three. In this figure vertical dashed lines are used to indicate the times at which ν_{OH} reaches its peak and $\nu_a(CH_3)$ rises to 90% of its maximum. The data indicate that each additional $-CH_2-$ unit increases the transfer time by ~0.4 ps. Additional methylene units also decrease the overall quantum yield for $\nu_{OH} \rightarrow \nu_a(CH_3)$ transfer.

Using 0.4 ps for the time and 1.5Å for the distance gives a velocity for vibrational excitations across methylene groups of 375 m/s. That is about the speed of a small calibre bullet, but more than a factor of three less than the speed of sound in ethanol. The reason this velocity is noticeably smaller than the acoustic velocity is that the energy transfer is not ballistic. At every step (see figure 5), an amount of energy of $\sim kT$ must be picked up or lost to the solvent, which limits the velocity in physical space [25].

4. Watching vibrational energy across an interface

In the past few years, several groups have studied reverse micelles with ultrafast vibrational spectroscopy [41–44]. In reverse micelles (depicted in figure 8) suspended in an organic solvent, an approximately spherical nanopool of water is confined by a surfactant monolayer [45]. The most commonly studied micelles are based on the surfactant 'Aerosol-OT' (AOT) which has a branched tail structure (see figure 8)

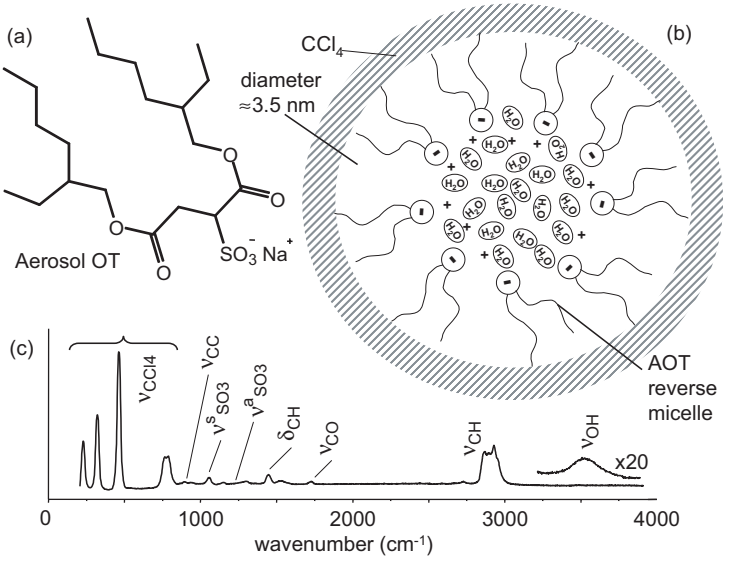

Figure 8. (a). Structure of AOT surfactant. (b). Schematic of a reverse micelle with water to AOT concentration of 2. (c). Assignments of the Raman spectrum of reverse micelles in CCl_4. Reproduced from ref. [24].

that promotes spherical interface formation. Micelle sizes are characterized by the water-to-AOT molecular ratio [45]. Increasing the water content increases micelle diameter.

Most work in this area has been devoted to understanding how the vibrational and orientational dynamics of confined water in AOT micelles differ from bulk water [41–44]. But because the confined water has such a high surface-to-volume ratio, it is also a useful model system for studying vibrational energy transfer and heat transfer across short distances. With IR-Raman techniques it becomes possible to measure not only the water vibrational dynamics, but the specific pathways of vibrational energy moving through the surfactant layer into the bulk solvent.

The flow of heat between two bulk phases separated by an interfacial monolayer is usually a simple function of the thermal conductivities of the bulk phases. G. Seifert and co-workers [46, 47] looked at AOT reverse micelles with a water to AOT ratio in the 10–55 range. They excited ν_{OH} of confined water. After thermalization, IR probe pulses were used to measure the rate of water cooling. Occurring over hundreds of picoseconds, the non-exponential cooling process and its dependence on micelle diameter could be explained with ordinary heat conduction theory for a hot water droplet suspended in a colder bath [47]. The thermal conductivity of the interfacial AOT layer was unimportant in this case because the rate-limiting step involved moving the heat out of the water nanopool, as opposed to moving heat across the interface.

However if the heat source is within a few molecular diameters of the interfacial layer, the interfacial thermal conductivity becomes important. The flow of vibrational energy across an interfacial monolayer can depend on how and where the energy is deposited in

the system, and in contrast to heat flow, different excitations may travel across the interface along different pathways and with different rates [24].

The role of an interfacial monolayer in vibrational energy transfer can be studied using AOT micelles with a small water-to-surfactant ratio, so that all the water molecules lie within a few molecular diameters of the surfactant layer. In our measurements a water-to-surfactant ratio of 2 was used. Most of the cited studies on AOT reverse micelles [41–44] used a hydrocarbon as the organic solvent, but in our experiments CCl_4 was chosen for its function as a molecular thermometer. Based on simulations and light scattering measurements of AOT/water/CCl_4 reverse micelles [48], our samples consisted of ~3.5 nm mean diameter micelles with an AOT mean aggregation number of 17–18, enclosing ~35 molecule water droplets ~1.3 nm in diameter. Based on our IR studies of the concentration-dependent ν_{OH} lineshape, analysed using methods described in ref. [49], we found that most of the confined water is interfacial water [45, 50, 51] bound or trapped near the AOT SO_3^- (sulfonate) head groups. There is little interior or 'bulk-like' water, as expected from experiments [49] and simulations [50] that indicate the interfacial water fraction is 70–80%.

Figure 8 [24] shows the Stokes Raman spectrum of the reverse micelle suspension. This spectrum shows the H_2O stretching and bending transitions, four CCl_4 Raman transitions, and several transitions of AOT including CH-stretching and CC stretching (since more than 90% of the ν_{CH} and ν_{CC} excitations are in the AOT tail we will call these 'tail excitations'), and the symmetric and antisymmetric stretching modes of the AOT sulfonate head group ν^s_{SO3} and ν^a_{SO3}. In light of recent advances in multidimensional vibrational spectroscopy, we might in retrospect term this ordinary Raman spectrum a 'one-dimensional' spectrum. In this 1D spectrum, which depends on the usual two-time correlation function $\langle\alpha(0)\alpha(t)\rangle$, there is no information associated with the transitions beyond their centre frequency, intensity and lineshape [52]. However, of course, we know from the micelle structure that the water transitions arise from the micelle interior, the AOT transitions from the interfacial layer and the CCl_4 transitions from the exterior. These factors will become evident from 3D IR-Raman spectra, which is sensitive to correlations between and among the different excitations.

We used IR pulses to pump either ν_{OH} of the confined water, or ν_{CH} of the AOT tail. The subsequent vibrational energy transfer processes are shown in figures 9 and 10 [24]. In figure 9 the movement of vibrational energy over time from water to AOT to CCl_4 is clearly evident. The traces in figure 11 reveal the dynamics extracted from the spectra in figures 9 and 10. The signal denoted NLS in figure 11 is a coherent artifact generated by nonlinear light scattering used to measure the apparatus time response, a Gaussian with 0.55 ps HWHM [53].

In figure 9, as energy leaves the ν_{OH} vibration a substantial portion passes into the ν^s_{SO3} and ν^a_{SO3} head group stretches: figure 11(a) shows $\nu_s(SO_3)$ excitation rising in 1.5 ps as ν_{OH} decays and then decaying with a T_1 of 6 ($\pm$1) ps. The sulfonate head group excitations are the predominant first-generation daughters of water VET; little AOT tail excitation is observed. In figure 10, the parent ν_{CH} excitations decay with a T_1 of 2.3 ($\pm$0.1) ps. The first-generation daughters include δ_{CH} and ν_{CC} tail excitations plus just a small amount of head group stretching. Fitting the data with a model of exponential build-up and decay gives effective lifetimes of 4.4 ps for δ_{CH} and 5–10 ps for ν_{CC}.

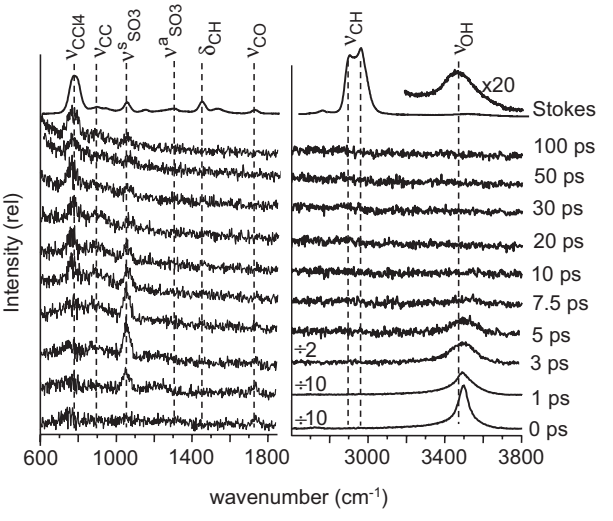

Figure 9. (top) Stokes Raman spectrum, with assignments, of AOT micelle suspension. From bottom to top: a time series of transient anti-Stokes spectra after OH stretch pumping of confined water at 3500 cm^{-1}. Reproduced from ref. [24].

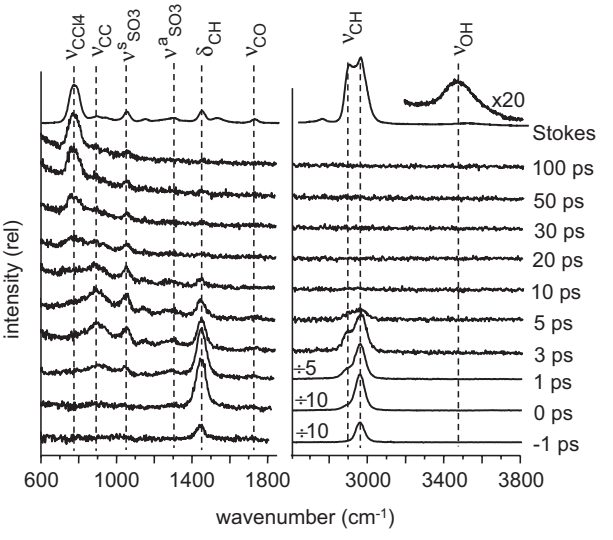

Figure 10. (top) Stokes Raman spectrum of AOT micelle suspension. From bottom to top: a series of transient anti-Stokes spectra (as in figure 9) acquired at successively longer delay times after CH stretch pumping of AOT at 2950 cm^{-1}. Reproduced from ref. [24].

Pumping the AOT ν_{CH} stretch leads to less head group excitation but much more AOT tail excitation than seen with water pumping [24].

Figure 11(c) details the rise of the 780 cm^{-1} signal from ν_2 of the CCl_4 molecular thermometer. After thermalization, ΔT was 5 K for water pumping and 16 K for AOT

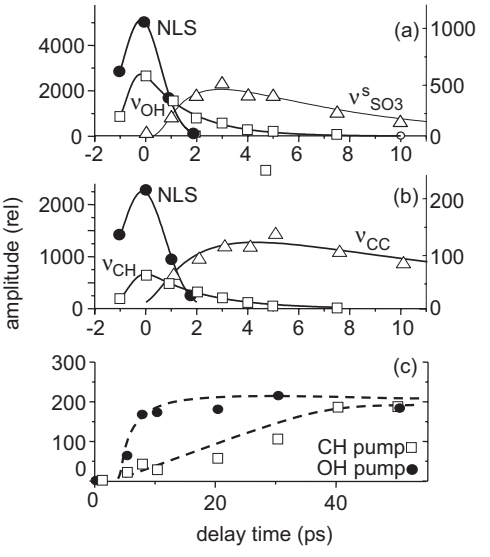

Figure 11. Dynamics extracted from figures 9 and 10. The NLS signal is a coherent artifact that tracks the apparatus-limited time response. The smooth curves are convolutions of the NLS signal with exponential build-up and decay functions. (a) Decay of the parent OH stretch ν_{OH} of water (left axis) and subsequent rise and decay of the symmetric stretch ν^{S}_{SO3} of the AOT head group (right axis). (b) Decay of the parent CH stretch ν_{CH} of AOT (left axis) and subsequent rise and decay of the AOT tail stretch ν_{CC} (right axis). (c) Rise of CCl_4 molecular thermometer after OH pumping of confined water and CH pumping of AOT. Reproduced from ref. [24].

pumping, and to facilitate comparison of the time dependences, the data in figure 11(c) were normalized to the same final amplitude. With water pumping most of the CCl_4 temperature rise occurs in the first 10 ps. With AOT tail pumping, the CCl_4 temperature does not begin to rise until ~20 ps, with equilibrium attained within ~40 ps.

If energy transfer from the reverse micelle to the surrounding CCl_4 operated through simple heat conduction, exciting the AOT tails would result in faster CCl_4 heating than exciting the confined water. But CCl_4 actually heats up faster with water excitation. This is a clear demonstration that molecular structures matter, in other words it is the specific molecular structures and vibrational relaxation pathways that determine vibrational energy flow over short distances.

A simple explanation for the disparity in solvent heating time scales has been developed [24], which provides a useful way to think about developing methods of controlling mechanical energy dissipation in nanostructures. This explanation is based on a paradigm first articulated by Nitzan and Jortner [54] in one of the first theoretical works examining the nature of vibrational relaxation of polyatomic molecules in condensed phases. These authors used the theory of radiationless transitions to derive an expression for the rate constant k for energy leaving an excited vibration with energy E,

$$k = \left(\frac{2\pi}{\hbar}\right)\langle V_{\text{anh}}\rangle^2 \rho(E), \tag{3}$$

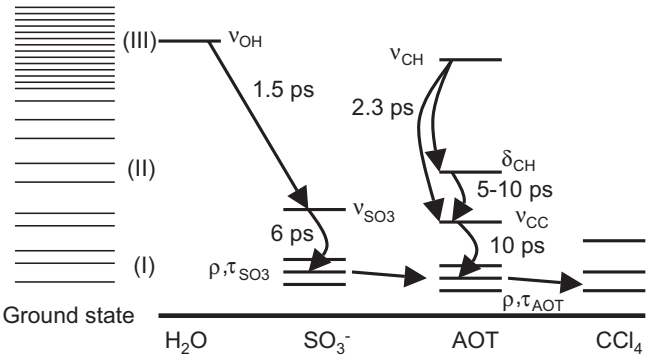

Figure 12. Energy level scheme for reverse micelles to explain why vibrational energy transfer is faster from water to CCl_4 than from AOT to CCl_4. (left) Three-regime model of Nitzan and Jortner [54]. Vibrational lifetimes are longest in regime II, where the state densities are lower and vibrations are predominantly harmonic. With ν_{OH} pumping, energy is conducted efficiently to the AOT sulfonate head group and then out into the solvent, spending little time in the longer-lived regime II vibrations. With ν_{CH} pumping, several longer-lived states in regime II are visited before energy moves out into the solvent.

where $\langle V_{anh} \rangle$ is the matrix element of the anharmonic coupling Hamiltonian and $\rho(E)$ is the vibrational density of states. From this starting point, the authors described how the vibrational lifetime $T_1 = (k)^{-1}$ varied with vibrational energy in three regimes (see the left hand side of figure 12). In the higher energy Regime III, the vibrations are approximately harmonic ($\langle V_{anh}$ is small) but the density of states $\rho(E)$ is quite large, so T_1 is shorter. In medium energy Regime II, vibrations are also approximately harmonic but the density of states is small, so T_1 is longer. In lower energy Regime I, the density of states is again small but vibrations are highly anharmonic, so T_1 is again shorter. On the basis of many studies of polyatomic CHON molecules in liquids [55], examples of Regime III vibrations would be CH or OH stretches or their overtones, and T_1 is typically in the range of 0.1–2 ps. Examples of Regime II vibrations would be CC stretch or CH bend, and T_1 is typically in the 2–50 ps range. Examples of Regime I vibrations would be methyl or nitro rocking or torsion, or skeletal or ring bending, and T_1 is typically in the 1–5 ps range.

Based on this scheme, a simple rule may be developed. When a significant amount of vibrational energy is loaded into a molecule, a complicated dissipation process results [56–60], but it is the fraction of energy in the longer-lived Regime II vibrations that ultimately determines the vibrational cooling rate. Figure 12 indicates our suggested pathways for VET from water to organic solvent and from AOT to organic solvent. With CH stretch pumping, a multistep vibrational cascade ensues, involving Regime II vibrations such as δ_{CH} and ν_{CH}. With multiple steps lasting perhaps 10 ps each, it takes about 40 ps for energy to leave the longer-lived states of Regime II. Although this was not observed, we presume that once the Regime II vibrations decay, short-lived Regime I vibrations are generated such as sulfonate torsions, scissors and rocking and large-amplitude skeletal stretching and bending modes of the AOT tails. These large-amplitude tail motions quickly and efficiently lose energy to CCl_4. With OH stretch pumping of water, there is an efficient intermolecular channel to stretching transitions of the sulfonate head groups from the associated water. Based on experience

with nitro groups [61, 62], the sulfonate stretching excitations decay into Regime I sulfonate torsions, scissors and rocking modes and AOT tail excitations, which transmit energy efficiently to CCl_4. So the direct water-to-sulfonate intermolecular transfer process bypasses most of the longer-lived states in Regime II that were populated by ν_{CH} relaxation, resulting in the fastest energy transfer across the surfactant monolayer.

5. Watching vibrational energy from an impact

When molecular materials are subjected to high-speed impact, a great deal of vibrational energy is created. This energy can induce explosive chemical reactions in the case of energetic materials [63–65], it can cause the molecules to deform in the case of viscoelastic media such as polymers, and it can cause brittle materials to undergo cracking and mechanical failure. Shock compression science has been a key intellectual development in our understanding of the response of materials to high-speed impact [66]. Shock experiments are typically performed in government or military labs, where gas guns are used to launch projectiles into a sample wired up with single-shot diagnostics having time resolution of 10 ns or more [67]. The repetition rate is a few shocks per week when everything goes well.

By way of contrast, ultrafast laser experiments such as the ones described above are performed at kHz repetition rates, and sophisticated spectroscopic diagnostics with high time and space resolution are used. In the Dlott lab, novel techniques have been developed to study shock compression of condensed matter using high-repetition-rate laser spectroscopies [67, 68]. These techniques involve the generation of tiny but powerful laser-driven shock waves, termed 'nanoshocks' [69, 70]. Typical shock velocities in condensed matter are a few $km\,s^{-1}$ or equivalently a few $\mu m\,ns^{-1}$ or $nm\,ps^{-1}$. Convenient kHz lasers generate pulse energies of ~1 mJ. In order to generate shocks with GPa pressures (1 Gpa ≈ 10 000 atm) using a portion of the pulse, say 0.1–0.5 mJ, the laser fluence should be $10^4\,J\,m^{-2}$, so the beam diameter will be ~200 μm. A shock emanating from a 200 μm diameter spot expands spherically, but 1D planar motion is greatly desired for ease of analysis [71]. A shock is conventionally viewed as 1D if the run distance is less than 10% of the diameter, so planar shock compression in this situation would be achieved over a run distance of ~10 μm [72]. Thus the 'nanoshock' name is derived from both the nanograms of material compressed and the nanoseconds of planar shock run [69, 70].

In ordinary laser pump-probe experiments, both pump and probe pulses propagate at the speed of light. In other words a sample is excited at the speed of light and probed at the speed of light. As long as dispersion is not a significant factor, the ultimate time resolution is limited by the laser pulse durations, not the thickness of the sample. However with nanoshock experiments, the sample is excited at the speed of shock (a bit greater than the speed of sound but nonetheless $\sim 10^5$ times slower than light speed) and probed at the speed of light. Thus a sample becomes excited at a relatively slow rate of $nm\,ps^{-1}$. If picosecond time resolution is to be obtained, the sample must be at most a few nanometers thick, so high space resolution is a prerequisite to high temporal resolution of shock compression effects [69, 70]. This problem has been

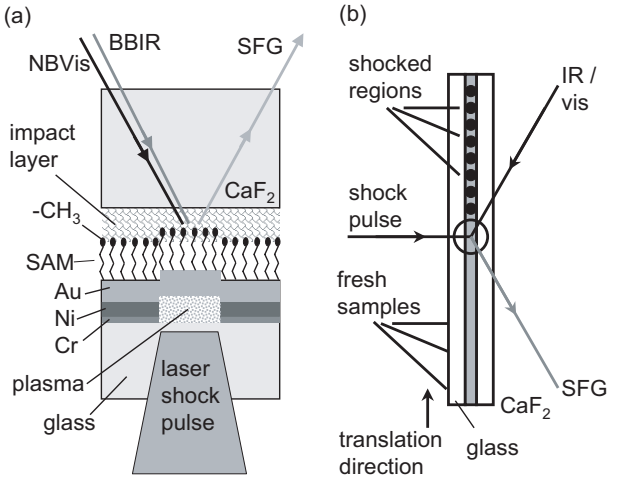

Figure 13. Shock target array. (a) Schematic of a single element. A laser drive pulse generates a 5–10 GPa shock in Ni that propagates through an impedance-matched Au layer before reaching the SAM, where the pressure drops to 1.3–1.6 GPa. The impact layer is perdeuterated ethylene glycol. Vibrational sum-frequency generation (SFG) spectroscopy monitors CH stretch transitions of the terminal methyl groups. (b) The shock target array is translated through the intersection of the shock generation pulse and the SFG probe pulses. Each laser shot hits a fresh sample. Adapted from ref. [73].

surmounted by fabricating samples with a sandwich structure, where the sandwich filling is a thin layer of the material of interest, which is spectroscopically unique [67].

In what is presumably the ultimate in high spatial resolution, shock compression effects in molecular materials have now been probed using a layer only one atom thick (in the sense that theorists frequently treat methyl groups as a single extended atom) [26, 73–75]. This is accomplished with a sandwich structure where the filling is an alkane–thiol SAM probed by SFG. In SFG measurements of well-ordered alkane SAMs, the methylene groups whose structure approximates that of a centrosymmetric crystal produce weak or negligible spectra, so SFG is a selective probe of the terminal methyl groups [76], which lie in a plane about 1.5 Å thick.

A nanoshock experiment irreversibly damages the sample. For high repetition rate measurements, experiments use a shock target array [77] such as the one illustrated in figure 13. Figure 13(a) depicts a single element of the array [26]. The laser shock pulse passes through a glass substrate and is partially absorbed by a Ni layer. A thin Cr layer is used as an adhesion promoter. At the glass–Ni interface, a laser plasma is generated. Rapid expansion of the plasma drives a shock into Ni and the adjacent Au layer. The shock generation and propagation process has been studied extensively by the group of D. Moore and D. Funk at Los Alamos National Laboratory [78–82]. In the experiments described below, the Ni plus Au plus Cr thickness is ~200 nm and the shock pressure in Ni and Au is 5–10 GPa. There is a large impedance mismatch between Au and the SAM, so the shock pressure drops to 1.3–1.6 GPa in the SAM [26, 73]. The SAM is compressed by 10–13% in the longitudinal direction. Figure 13(b) depicts the multi-element target array [26, 73], which is $50 \times 50\,\text{mm}^2$. Since individual array elements are $200 \times 200\,\mu\text{m}^2$, a single target array on an *xy* translator

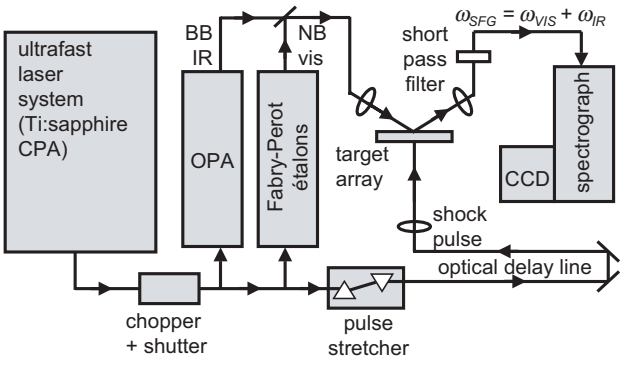

Figure 14. Schematic of the optical setup used for the laser shock experiments. CPA = chirped-pulse amplifier; OPA = optical parametric amplifier; CCD = charge-coupled array detector; BBIR = broad band mid-IR pulse; NBvis = narrow-band visible pulse. Adapted from ref. [73].

supports ~50K nanoshock events. Typically this would represent spectra accumulated over ~1–5K shots and ~10–50 different values of the delay time.

A block diagram of the laser system [26, 73] is shown in figure 14. The amplified femtosecond pulse is split into three parts. One part pumps the IR OPA and one part is spectrally narrowed by passing through an étalon, to produce the two pulses needed for SFG. The third part is the shock driver pulse, which is stretched to ~1 ps. Stretching the pulse allows one to propagate more energy through the glass substrate (see figure 13) without dielectric breakdown [78, 83].

From the point of view of the terminal methyl groups, it is as if the Au baseplate underneath has suddenly become a hammer head moving at a high velocity of > 100 m/s. This deforms the SAM chains and drives the methyl groups into the impact layer, which in these experiments consisted of deuterated ethylene glycol.

In order to gain insight into what happens to SAMs under shock compression, a commercial molecular mechanics package was used to simulate [26, 84] slow isothermal compression of the SAMs depicted in figure 15 having either an odd number (pentadecyl thiol = $HS(CH_2)_{14}CH_3$ = PDT, with 15 carbon atoms) or an even number of carbon atoms (octadecyl thiol = $HS(CH_2)_{17}CH_3$ = ODT, with 18 carbons). Extensive past studies of SAMs have shown that both ODT and PDT fall into the long-chain limit, generally taken to be $\geq$14 carbon atoms [56–58]. The methyl tilt angle θ is defined in figure 16(a); it is the angle between the methyl C_{3v} axis and the surface normal. Due to the zigzag alternation of the all-*trans* chains which have similar chain tilt angles of 35°, with ODT the terminal methyl is nearly upright with $\theta = 23°$; for PDT the methyl is more tilted, with $\theta = 65°$.

Chain alternation is found to have a substantial effect on the way chains respond to compression. The PDT chains respond mainly by a combination of methyl tilting and whole-chain tilting [26, 84]. The simulations thus suggested that PDT shock compression should be an elastic process, and that when the shock load decays away the PDT chains should instantaneously reorient to their original conformation. The ODT chains are more susceptible to a mechanical failure process which results in the formation of *gauche* defects [26, 84]. *Gauche* defects are created by rotation around the

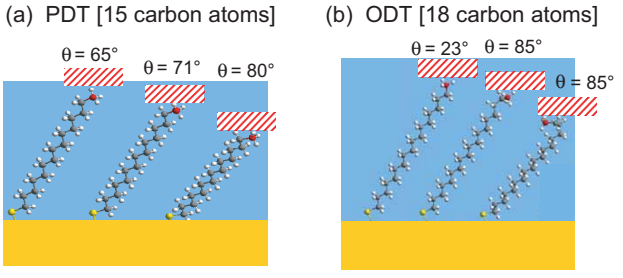

Figure 15. [Colour online] Response of long-chain alkane SAMs to gradual isothermal compression. The SAM model used supercells of PDT $[CH_3(CH_2)_{14}SH]$ and ODT $[CH_3(CH_2)_{17}SH]$ molecules on a $(\sqrt{3} \times \sqrt{3})R30^\circ$ lattice on Au(111) [104] with periodic boundary conditions, but for clarity only single chains are shown here. The methyl tilt angle θ is defined in figure 16(a). (a) PDT chains with an odd number of carbon atoms have a larger tilt angle, and when compressed the tilt gradually increases as a result of methyl tilting and whole-chain tilting. (b) ODT chains with an even number of carbon atoms have more upright methyl groups and are more susceptible to *gauche* defect creation. The conformers shown here with single and double gauche defects have higher tilt angles. Adapted from ref. [84].

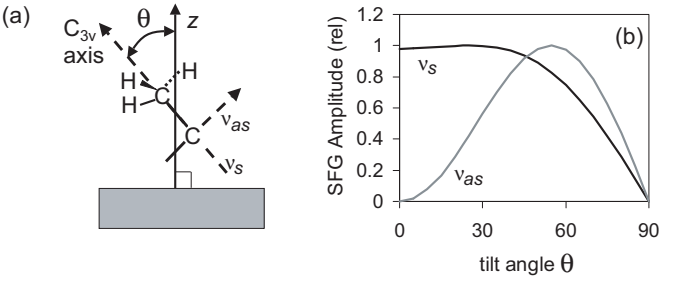

Figure 16. (a) The methyl tilt angle θ for alkanes ODT and PDT is the angle between the surface normal and the methyl C_{3V} axis. (b) Calculated CH-stretch SFG amplitude as a function of tilt angle. Adapted from ref. [84].

C–C dihedrals, and energetically it was found most favourable to create *gauche* defects at the first and second dihedrals below the terminal methyl [26, 84]. Using *t* to denote *trans* and *g* for *gauche*, the initial all-trans configuration is *ttt*. Three-letter combinations are used since dihedrals below the third are assumed to be all-*trans* [26, 84]. There are barriers to rotation around the dihedrals in most cases, so when the shock load decays away *gauche* defects in ODT may be metastable and may persist for an indeterminate time.

Using SFG with the *ppp* polarization condition [18, 21, 26], it is possible to determine the instantaneous methyl tilt angle defined in figure 16(a), using the relative intensities of the ν_sCH and ν_{as}CH transitions [26, 73]. The relationship between SFG intensity and methyl tilt angle shown in figure 16(b) was calculated using equations developed by Hirose *et al.* [85, 86], with the usual assumption that $-CH_3$ is a free rotor. Three notable points of this calculation: (1) with ODT where methyl groups are nearly upright, ν_s will be more intense than ν_{as}; (2) with PDT having more tilted methyl groups, ν_s and ν_{as} intensities will be similar; (3) at large tilt angles suggested by figure 15, *both* ν_s *and* ν_{as} *intensities will be small*. SFG spectra of PDT and ODT without shock

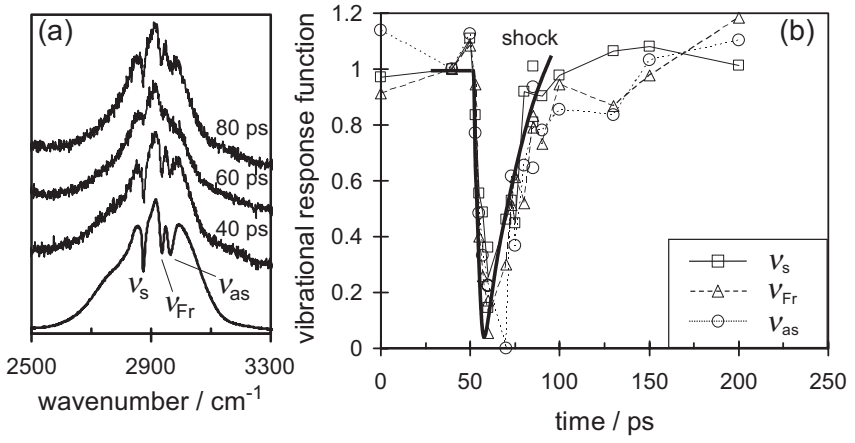

Figure 17. (a) SFG spectra of PDT on Au with shock compression. The bottom spectrum is obtained without shock, with extensive integration time. The shock front arrives at the monolayer surface ~50 ps after time zero denoting the arrival of the shock-generation laser pulse. (b) Time-dependent SFG intensities of three PDT transitions, plotted as normalized vibrational response functions (equation 4). The curve labeled 'shock' is the time-dependent envelope of the nanoshock. SFG signal loss and recovery closely track the shock envelope, indicating that PDT on Au shock compression is largely an elastic tilting process. Reproduced from ref. [73].

compression are shown at the bottom of figures 17(a) and 18(a). With SAMs on Au and 800 nm visible pulses, the CH stretch transitions appear as ~15 cm^{-1} FWHM dips in a non-resonant background whose shape mirrors the spectrum of the IR pulses. As expected, the ν_s/ν_{as} ratio is quite a bit larger in ODT. The transition denoted ν_{FR} has primarily bending overtone character; its intensity is enhanced by Fermi resonance and we do not have a quantitative model for the tilt-angle dependence of its SFG intensity.

Figures 17 and 18 show the dynamical effects of shock compression on PDT and ODT SAMs [26, 73]. In these figures, $t = 0$ denotes the arrival of the shock-generating laser pulse at the sample. At about 50 ps, there is a sudden loss of intensity, occurring in < 4 ps, of the sharper dips in the SFG spectra that denote CH-stretch transitions. This intensity loss was shown definitively to result from the arrival of the shock front at the SAM [26, 73]. A series of experiments were performed where the thickness of the Au layer was increased in ~10 nm increments; the onset of this sudden intensity drop was thereby delayed by times that were consistent with the ~3 nm/ps velocity of small-amplitude shocks in Au [73].

In order to characterize the shock-induced intensity loss, a normalized vibrational response function $I(t)$ was defined [26, 73]. The depths of the resonant features in the unshocked spectrum, I_{ns}, and in the shocked spectrum at delay time t, $I_s(t)$, were measured and each normalized to the overall height of the non-resonant SFG signal, I_{nr}, then combined to give

$$I(t) = \frac{[I_s(t)/I_{nr}]}{[I_{ns}/I_{nr}]}. \tag{4}$$

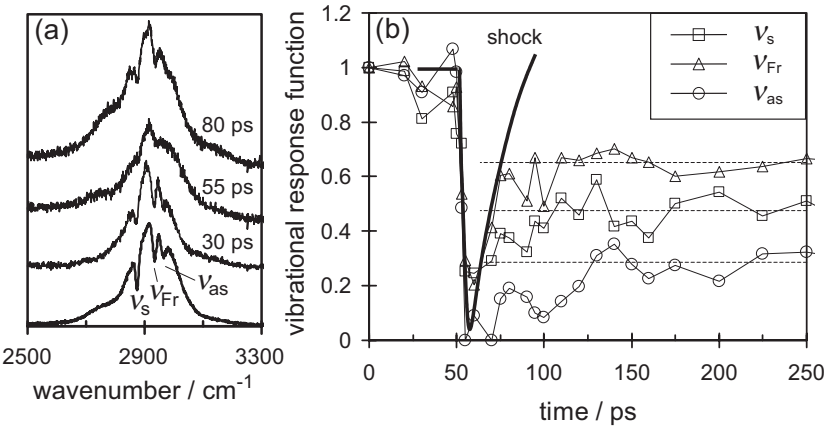

Figure 18. (a) SFG spectra of ODT on Au with shock compression. (b) Time-dependent vibrational response functions for three ODT transitions. Shock compression results in a persistent loss of SFG signal for ODT, and an enhancement in the ν_s/ν_{as} ratio, indicating the shock creates some high-tilt SFG-invisible conformers and some confomers with nearly upright terminal methyl groups. Reproduced from ref. [73].

As shown in figures 17 and 18, the sudden intensity loss effect is similar with both PDT and ODT, but the subsequent intensity recovery effect is quite different [26, 73]. In PDT the CH-stretch intensities recovery is approximately exponential in time with a time constant of ~15 ps. This decay is close to what was expected for the decay of the nanoshock pressure, which occurred when the release wave from the metal film catches up to the shock front. In ODT, there was only a partial intensity recovery occurring over ~30 ps. At times longer than ~1 ns, the shocked sample broke up into pieces and SFG spectra could not be obtained, so the loss of SFG intensity is determined to persist until at least 1 ns.

Interpreting the vibrational response in terms of methyl tilt gives the following picture. Shock front arrival causes a tilt of the terminal methyl groups to a large angle near 90°, which is the only angle where both ν_s and ν_{as} intensities vanish. The shock-induced deformation of PDT is an elastic process, and the PDT intensities recover instantaneously (in the sense that they follow the expected curve for shock pressure decay). The complete recovery of PDT signals indicates that shock compression at the levels produced here does not cause SAM chains to desorb from the Au substrate. Shock-induced deformation of ODT results in a long-lasting deformation of the alkane chains. As suggested by figure 15, we attribute this effect to the formation of *gauche* defects. At longer times in figure 18(b), the ν_{as} intensity has not recovered as much as the ν_s intensity, in other words the longer-term effects of shock compression have been to increase the ν_s/ν_{as} ratio. These observations suggest that shock compression has generated at least two new metastable species, one that is nearly SFG-invisible and one that is nearly upright. As a result of simulations such as those described in figure 15, we have postulated that shock compression creates a mixture of single and double *gauche* defects $-gtt$ and $-g+gt$ [26, 84]. The preference for $-g$ configurations is a consequence of the initial tilt angle (see figure 15); creating $+g$ configurations would require the chains to bend in the wrong direction [84]. Both $-gtt$

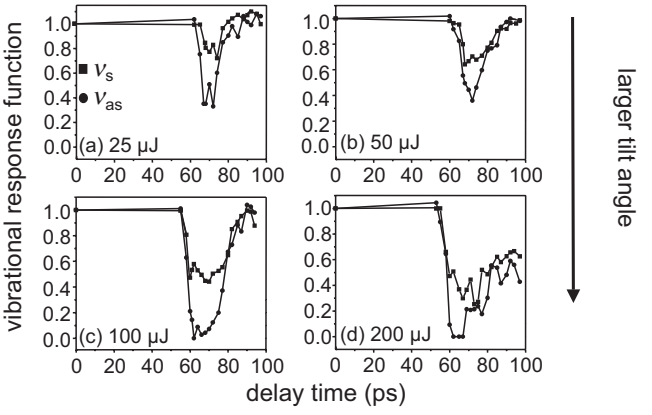

Figure 19. SFG signals from ODT shocked with 840 fs duration pulses at the indicated energies. Reproduced from ref. [83].

and $-g+gt$ (depicted in figure 15) have large methyl tilt angles near 85° and are nearly SFG invisible [84], which accounts for the nearly complete loss of SFG intensity at the shock front. When the shock unloads, $-gtt$ has a barrier to reconversion to ttt, but $-g+gt$ has a minimal barrier to conversion into the nearly upright $t+gt$ conformer with a methyl tilt angle of just 12°. Thus the two effects seen at longer times in ODT, the persistent loss of intensity and the enhancement in the ν_s/ν_{as} ratio, are attributed to shock-induced creation of (almost invisible) $-g+gt$ and (nearly upright) $t+gt$ conformers.

Figure 19 illustrates the effects of increasing the shock strength with ODT [83]. The shock strength is varied by changing the energy of the laser drive pulses. With the weakest drive pulses (figure 19a), the SFG signal drop is only partial, and the signals recover completely. Figures 19(b,c) show that increasing the drive pulse energy causes a larger loss of SFG intensity that persists for a somewhat longer time. Figure 19(d) is approximately the same condition used in figure 18, which caused a persistent loss of SFG intensity.

The shock front rise time can be estimated from the <4 ps SFG signal loss effect [73]. Some of the observed time constant may result from surface roughness causing a spread of shock front arrival times [87], and some from the intrinsic time resolution of the SFG probe. Using atomic-force microscopy, we have determined that the Au surface has an RMS roughness of 4 nm [83]. This roughness averaged over the beam profile and over many laser shots should result in an $\sim$1.3 ps spread in shock front arrival times. The time response of SFG is approximately equal to the decay time of the vibrational coherence of the CH stretch transitions [26]. The coherence decay time constant T_2 can be estimated from the linewidth $\Delta\nu$ of the CH stretching resonances, using the relation, $T_2=(\pi\nu_{1/2})^{-1}$. For SAMs with $\nu_{1/2}\approx 15\,\mathrm{cm}^{-1}$, $T_2\sim 0.7$ ps, so the intrinsic time resolution of the SFG probe is $\sim$1.4 ps. The usual way to combine all these finite time effects is to convolve Gaussian functions representing each contribution [88]. Using this procedure with the <4 ps observed rise time, the 1.3 ps arrival time dispersion, and the 1.4 ps vibrational dephasing gives a shock front rise time of $t_r < 3.5$ ps.

The SFG and SAM system combined with femtosecond laser shock generation is a technology platform that can be used to investigate the fast response of molecules to high strain rates associated with high-speed impact or high-speed moving surfaces. In the ODT experiments, deformations of all-*trans* alkane chains were created by rotation around carbon–carbon bonds on the time scale of ~4 ps. In some ways this development in shock compression science parallels earlier developments in ultrafast spectroscopy, albeit with a lag time of 25–30 years. In about the year 1980, researchers conducted important studies on condensed phase molecular reaction dynamics using photo-induced *cis*-to-*trans* isomerization of polyenes such as stilbene [89] or rhodopsin [90], with ~2 ps duration laser pulses. As shown subsequently, an entirely new regime of chemical reactivity can be observed when femtosecond pulses, rather than picosecond pulses are used [91–94]. This is because the vibrational periods associated with the motions needed to surmount barriers to isomerization are about 10^{-13} s. With picosecond excitation photoisomerization is an incoherent process, where different molecules surmount the barrier at different times. But with femtosecond pulses isomerization is a coherent process where all molecules surmount the barrier at the same instant [93]. It is to be expected that a corresponding new regime of shock compression could also be attained if the condition $t_r < t_{tr}$ could be achieved, where t_r is the rise time of the shock front and t_{tr} is the shock transit time across the molecule [95]. In the monolayer work described here, this condition is not achieved, $t_r > t_{tr}$ where $t_r \approx 4$ ps and $t_{tr} \approx 1$ ps. In this case, as illustrated in figure 20(a), stress and strain build up almost uniformly over the length of the alkane chain. The alkane chains are gradually squeezed in a vise until they undergo mechanical failure. However if shorter duration shock fronts could be generated, it should be possible to create large strains that propagate through the molecule, as illustrated in figure 20(b). In this case the shock front ought to be steep enough to coherently drive molecular vibrational excitations [95–98].

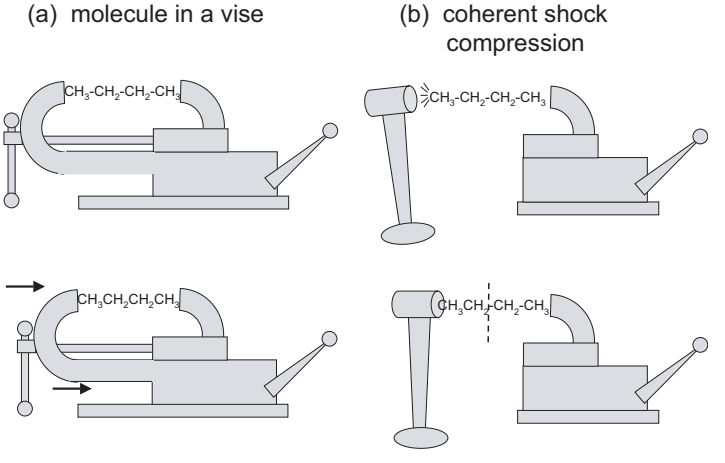

Figure 20. Depiction of coherent and incoherent shock compression. (a) When $t_r > > t_{tr}$, where t_r is the shock front rise time and t_{tr} the shock transit time across the molecule, shock compression increases gradually, as if the molecules were compressed in a vise. (b) When $t_r \leq t_{tr}$ the molecule is struck a sharp blow, as if with a hammer. Behind the shock front large amounts of vibrational energy are input to specific modes that strongly couple with translational motions.

Large amounts of vibrational excitation would be rapidly input into specific modes – those modes which couple most efficiently to translational excitations. Since the rate of energy input is expected to be faster than the rates of vibrational energy redistribution, new chemistries that differ from thermal or photo chemistries might be observed [95]. Each time new technologies having better time resolution have been introduced in shock compression science, measured shock front rise times have appeared shorter in duration. However in the latest femtosecond measurements rise times remain fixed in the few picosecond range. Shock front atomistic simulations frequently show much faster structures at shock fronts [99], suggesting that faster shocks may be attainable. Novel generation methods that combine shaped laser pulses, thinner shock generation layers and shock focusing techniques are currently being explored in order to see if the shock compression analog of femtochemistry might someday be developed.

6. Concluding remarks

We have described new measurements of vibrational energy in molecular liquids and molecular nanostructures. Now we briefly discuss the implications. The role of vibrational energy in chemical reaction dynamics is well recognized. Work such as ours, which provides a unified overview of vibrational energy by probing the parent vibration and daughter vibrations on the laser-excited molecule and its neighbours, is particularly suited to the task of building conceptual frameworks. In addition our work provides useful benchmarks to assist the development of computational models for VER. An excellent example of this is found in the work [100] of Gulmen and Sibert III at Wisconsin, who have performed detailed calculations of the VER processes in liquid methanol corresponding to figure 3. This work is based on classical simulations but incorporates quantum effects at the level of Landau–Teller theory. Computational studies of VER of methanol, a molecule with six atoms plus the additional complications of molecular association through hydrogen-bonding, are at the very edge of what is possible today.

We began this review with a brief discussion of heat dissipation, so it is fitting to return to this topic now. Every machine requires heat dissipation to function, and naturally engineers have become experts in classical heat transport. As nanotechnology evolves and machines continue to shrink in size, designers will face similar dissipation issues which will obey more complicated rules that are only now being investigated. Biological molecular machines operate at relatively low repetition rates, typically less than 1 kHz, so vibrational energy build-up is probably not important. However there have been studies that suggest the non-equilibrium effects resulting from a burst of vibrational energy [101] associated with substrate binding or dissociation might have an effect on biological machines, for instance studies by J. M. Friedman [102] and W. A. Eaton [103] of cooperative structural changes in hemoglobin. Electrical engineers concerned with building smaller faster electronic circuits at GHz and higher repetition rates are now confronting difficult issues of short-length scale heat dissipation, so it can be imagined that the development of molecular nanomachines operating near theoretical speed limits will require clever designs to optimize the transport of vibrational energy through space.

Acknowledgements

The research described in this review is based on work supported by several funding agencies including the US Department of Energy through the Stewardship Sciences Academic Alliance Program from the Carnegie-DOE Alliance Center under Award No. DE-FC03-03NA00144 and through the Frederick Seitz Materials Research Laboratory and the Center for Microanalysis of Materials at the University of Illinois at Urbana-Champaign under Award No. DEFG02-91ER45439. Additional support was provided by the National Science Foundation under award DMR-05-04038, the US Air Force Office of Scientific Research under award number FA9550-06-1-0235 and the US Army Research Office under contract W911NF-05-1-0345. JCD acknowledges a Cottrell College Science Award from the Research Corporation.

References

[1] N. W. Ashcroft and N. D. Mermin, *Solid State Physics* (Holt, Reinhart and Winston, New York, 1976).
[2] P. G. Klemens, in *Solid State Physics*, edited by F. Seitz and D. Turnbull (Academic Press, New York, 1958) Vol. 7, p. 1.
[3] D. D. Joseph and L. Preziosi, Rev. Mod. Phys. **61,** 41 (1989).
[4] S. Califano, V. Schettino, and N. Neto, *Lattice Dynamics of Molecular Crystals* (Springer-Verlag, Berlin, 1981).
[5] V. M. Kenkre, A. Tokmakoff, and M. D. Fayer, J. Chem. Phys. **101,** 10618 (1994).
[6] A. Laubereau and W. Kaiser, Rev. Mod. Phys. **50,** 607 (1978).
[7] D. W. Oxtoby, in *Photoselective Chemistry Part 2*, edited by J. Jortner, R. D. Levine, and S. A. Rice (Wiley, New York, 1981) Vol. 47, p. 487.
[8] M. D. Fayer, *Ultrafast Infrared and Raman Spectroscopy* (Marcel Dekker, New York, 2000).
[9] L. Iwaki and D. D. Dlott, in *Encyclopedia of Chemical Physics and Physical Chemistry*, edited by J. H. Moore and N. D. Spencer (IOP Publishing Ltd., London, 2001), p. 2717.
[10] R. Rey, K. B. Møller, and J. T. Hynes, Chem. Rev. **104,** 1915 (2004).
[11] A. Laubereau, L. Greiter, and W. Kaiser, Applied Physics Letters **25,** 87 (1974).
[12] A. Seilmeier and W. Kaiser, in *Ultrashort Laser Pulses and Applications*, edited by W. Kaiser (Springer Verlag, Berlin, 1988) Vol. 60, p. 279.
[13] K. Spanner, A. Laubereau, and W. Kaiser, Chem. Phys. Lett. **44,** 88 (1976).
[14] K. B. Eisenthal, Annu. Rev. Phys. Chem. **43,** 627 (1992).
[15] K. B. Eisenthal, Chem. Rev. **1343,** (1996).
[16] K. B. Eisenthal, Chem. Rev. **106,** 1462 (2006).
[17] G. L. Richmond, Chem. Rev. **102,** 2693 (2002).
[18] Y. R. Shen, Nature **337,** 519 (1989).
[19] Y. R. Shen, Surface Science **299/300,** 551 (1994).
[20] A. Tadjeddine, Surf. Rev. and Lett. **7,** 423 (2000).
[21] L. J. Richter, T. P. Petralli-Mallow, and J. P. Stephenson, Opt. Lett. **23,** 1594 (1998).
[22] E. W. M. van der Ham, Q. H. F. Vrehen, and E. R. Eliel, Opt. Lett. **21,** 1448 (1996).
[23] S. Roke, A. W. Kleyn, and M. Bonn, J. Phys. Chem. A **105,** 1683 (2001).
[24] J. C. Deàk, Y. Pang, T. D. Sechler, Z. Wang, and D. D. Dlott, Science **306,** 473 (2004).
[25] Z. Wang, A. Pakoulev, and D. D. Dlott, Science **296,** 2201 (2002).
[26] J. E. Patterson, A. S. Lagutchev, W. Huang, and D. D. Dlott, Phys. Rev. Lett. **94,** 015501 (2005).
[27] J. C. Deàk, L. K. Iwaki, and D. D. Dlott, Opt. Lett. **22,** 1796 (1997).
[28] J. C. Deàk, L. K. Iwaki, S. T. Rhea, and D. D. Dlott, J. Raman Spectrosc. **31,** 263 (2000).
[29] L. K. Iwaki and D. D. Dlott, J. Phys. Chem. A **104,** 9101 (2000).
[30] Z. Wang, A. Pakoulev, Y. Pang, and D. D. Dlott, J. Phys. Chem. **108,** 9054 (2004).
[31] Z. Wang, A. Pakoulev, Y. Pang, and D. D. Dlott, in *Femtochemistry and Femtobiology. Ultrafast Events in Molecular Science*, edited by M. M. Martin and J. T. Hynes (Elsevier, Amsterdam, 2004), p. 169.
[32] D. D. Dlott, Chem. Phys. **266,** 149 (2001).
[33] L. K. Iwaki and D. D. Dlott, Chem. Phys. Lett. **321,** 419 (2000).
[34] P. B. Graham, K. J. M. Matus, and R. M. Stratt, J. Chem. Phys. **121,** 5348 (2004).
[35] T. Förster, Ann. Phys. **6,** 55 (1948).

[36] B. Schrader, *Raman/Infrared Atlas of Organic Compounds*, 2nd ed. (VCH, Weinheim, 1989).
[37] J.-P. Perchard and M.-L. Josien, J. Chim. Phys. (Paris) **65,** 1834 (1968).
[38] G. A. Voth and R. M. Hochstrasser, J. Phys. Chem. **100,** 13034 (1996).
[39] A. Nitzan, S. Mukamel, and J. Jortner, J. Chem. Phys. **63,** 200 (1975).
[40] J. S. Hutchinson, W. P. Reinhardt, and J. T. Hynes, J. Chem. Phys. **79,** 4247 (1983).
[41] D. Cringus, J. Lindner, M. T. W. Milder, M. S. Pshenichnikov, P. Vöhringer, and D. A. Wiersma, Chem. Phys. Lett. **408,** (2005).
[42] A. M. Doktor, S. Woutersen, and H. J. Bakker, Phys. Rev. Lett. **94,** 178301 (2005).
[43] I. R. Piletic, H. S. Tan, and M. D. Fayer, J. Phys. Chem. B **109,** 21273 (2005).
[44] H. S. Tan, I. R. Piletic, R. E. Riter, N. E. Levinger, and M. D. Fayer (2004), unpublished.
[45] T. K. De and A. Maitra, Adv. Colloid Interface Sci. **59,** 95 (1995).
[46] T. Patzlaff, M. Janich, G. Seifert, and H. Graener, Chem. Phys. **2000,** 381 (2000).
[47] G. Seifert, T. Patzlaff, and H. Graener, Phys. Rev. Lett. **88,** 1 (2002).
[48] B. Derecskei, A. Derecskei-Kovacs, and Z. A. Schelly, Langmuir **15,** 1981 (1999).
[49] G. Onori and A. Santucci, J. Phys. Chem. **97,** 5430 (1993).
[50] J. Faeder and B. M. Ladanyi, J. Phys. Chem. B **104,** 1033 (2000).
[51] D. Brown and J. H. R. Clarke, J. Phys. Chem. **92,** 2881 (1988).
[52] S. Mukamel, *Principles of Nonlinear Optical Spectroscopy* (Oxford University Press, New York, 1995).
[53] A. Pakoulev, Z. Wang, Y. Pang, and D. D. Dlott, Chem. Phys. Lett. **380,** 404 (2003).
[54] A. Nitzan and J. Jortner, Molec. Phys. **25,** 713 (1973).
[55] D. D. Dlott, in *Laser Spectroscopy of Solids II*, edited by W. Yen (Springer Verlag, Berlin, 1988), p. 167.
[56] J. R. Hill, E. L. Chronister, T.-C. Chang, H. Kim, J. C. Postlewaite, and D. D. Dlott, J. Chem. Phys. **88,** 949 (1988).
[57] J. R. Hill, E. L. Chronister, T.-C. Chang, H. Kim, J. C. Postlewaite, and D. D. Dlott, J. Chem. Phys. **88,** 2361 (1988).
[58] J. R. Hill, E. L. Chronister, J. C. Postlewaite, and D. D. Dlott, Springer Ser. Phys. **46,** 482 (1986).
[59] J. R. Hill and D. D. Dlott, J. Chem. Phys. **89,** 830 (1988).
[60] J. R. Hill and D. D. Dlott, J. Chem. Phys. **89,** 842 (1988).
[61] S. Chen, X. Hong, J. R. Hill, and D. D. Dlott, J. Phys. Chem. **99,** 4525 (1995).
[62] J. C. Deàk, L. K. Iwaki, and D. D. Dlott, J. Phys. Chem. A **103,** 971 (1999).
[63] C. S. Coffey and E. T. Toton, J. Chem. Phys. **76,** 949 (1982).
[64] D. D. Dlott and M. D. Fayer, J. Chem. Phys. **92,** 3798 (1990).
[65] A. Tokmakoff, M. D. Fayer, and D. D. Dlott, J. Phys. Chem. **97,** 1901 (1993).
[66] R. A. Graham, *Solids Under High-Pressure Shock Compression. Mechanics, Physics and Chemistry* (Springer-Verlag, New York, 1993).
[67] D. D. Dlott, Annu. Rev. Phys. Chem. **50,** 251 (1999).
[68] D. D. Dlott, Acc. Chem. Res. **33,** 37 (2000).
[69] S. A. Hambir, J. Franken, and D. D. Dlott, High Pressure Sci. Technol. **7,** 891 (1998).
[70] G. Tas, S. A. Hambir, J. Franken, D. E. Hare, and D. D. Dlott, J. Appl. Phys. **82,** 1080 (1997).
[71] J. Cagnoux, P. Chartagnac, P. Hereil, and M. Perez, Ann. Phys. Fr. **12,** 451 (1987).
[72] Y. Yang, S. A. Hambir, and D. D. Dlott, Shock Waves **11,** 129 (2002).
[73] A. S. Lagutchev, J. E. Patterson, W. Huang, and D. D. Dlott, J. Phys. Chem. B **109,** 5033 (2005).
[74] J. Patterson, A. S. Lagutchev, and D. D. Dlott, AIP Confer. Proc. **706**, 1299 (2004).
[75] J. E. Patterson, A. S. Lagutchev, S. A. Hambir, W. Huang, H. Yu, and D. D. Dlott, Shock Waves **14,** 391 (2005).
[76] A. L. Harris, C. E. D. Chidsey, N. J. Levinos, and D. N. Loiacono, Chem. Phys. Lett. **141,** 350 (1987).
[77] S. A. Hambir, J. Franken, D. E. Hare, E. L. Chronister, B. J. Baer, and D. D. Dlott, J. Appl. Phys. **81,** 2157 (1997).
[78] S. D. McGrane, D. S. Moore, D. J. Funk, and R. L. Rabie, Appl. Phys. Lett. **80,** 3919 (2002).
[79] D. J. Funk, D. S. Moore, J. H. Reho, K. T. Gahagan, S. D. McGrane, and R. L. Rabie, AIP Conf. Proc. **620**, 1227 (2002).
[80] D. J. Funk, D. S. Moore, and K. T. Gahagan, Phys. Rev. B. **64,** 115114 (2001).
[81] D. S. Moore, K. T. Gahagan, S. J. Buelow, R. L. Rabie, D. J. Funk, S. A. Sheffield, L. L. Davis, T. Lippert, H. Brand, and J. W. Nicholson, AIP Conf. Proc. **505**, 1003 (2000).
[82] K. T. Gahagan, D. S. Moore, D. J. Funk, R. L. Rabie, S. J. Buelow, and J. W. Nicholson, Phys. Rev. Lett. **85,** 3205 (2000).
[83] W. Huang, J. E. Patterson, A. Lagutchev, and D. D. Dlott, AIP Confer. Proc. **845**, 1265 (2006).
[84] J. E. Patterson and D. D. Dlott, J. Phys. Chem. B **109,** 5045 (2005).
[85] C. Hirose, N. Akamatsu, and K. Domen, J. Chem. Phys. **96,** 997 (1992).
[86] C. Hirose, N. Akamatsu, and K. Domen, Appl. Spectrosc. **46,** 1051 (1992).
[87] S. A. Hambir, H. Kim, D. D. Dlott, and R. B. Frey, J. Appl. Phys. **90,** 5139 (2001).
[88] G. R. Fleming, *Chemical Applications of Ultrafast Spectroscopy* (Oxford University Press, Oxford, 1986).

[89] B. I. Greene, R. M. Hochstrasser, and R. B. Weisman, Chem. Phys. Lett. **62,** 427 (1979).
[90] C.-L. Hsieh, M. Nagumo, M. Nicol, and M. A. El-Sayed, J. Phys. Chem. **85,** 2714 (1981).
[91] R. W. Schoenlein, L. A. Peteanu, R. A. Mathies, and C. V. Shank, Science **254,** 412 (1991).
[92] B. I. Greene and R. C. Farrow, J. Chem. Phys. **78,** 3336 (1983).
[93] S. Pedersen, L. Banares, and A. H. Zewail, J. Chem. Phys. **97,** 8801 (1992).
[94] R. J. Sension, S. T. Repinec, A. Z. Szarka, and R. M. Hochstrasser, J. Chem. Phys. **98,** 6291 (1993).
[95] D. D. Dlott, in *Energetic Materials: Initiation, Decomposition and Combustion, Part 2*, edited by P. Politzer and J. S. Murray (Elsevier, New York, 2003), p. 125.
[96] J. Dancz and S. A. Rice, J. Chem. Phys. **67,** 1418 (1977).
[97] D. D. Dlott, in *Overviews of Recent Research on Energetic Materials*, edited by D. Thompson, T. Brill, and R. Shaw (World Scientific, New Jersey, 2005), p. 303.
[98] D. A. Rose and C. C. Martens, J. Phys. Chem. A **101,** 4613 (1997).
[99] B. L. Holian, Shock Waves **13,** 489 (2004).
[100] T. S. Gulmen and E. L. Sibert, J. Phys. Chem. A **108,** 2389 (2004).
[101] A. Ansari, J. Berendzen, S. F. Bowne, H. Frauenfelder, I. E. T. Iben, T. B. Sauke, E. Shyamsunder, and R. D. Young, Proc. Natl. Acad. Sci. USA **82,** 5000 (1985).
[102] J. M. Friedman, D. L. Rousseau, and M. R. Ondrias, Annu. Rev. Phys. Chem. **33,** 471 (1982).
[103] J. Hofrichter, J. H. Sommer, E. R. Henry, and W. A. Eaton, Proc. Natl. Acad. Sci. USA **80,** 2235 (1983).
[104] F. Bensebaa, T. H. Ellis, A. Badia, and R. B. Lennox, Langmuir **14,** 2361 (1998).